Hydrothermal Synthesis: A Suitable Route to Elaborate Nanomanganites

A. Querejeta,[†] A. Varela,[†] M. Parras,[†] F. del Monte,[‡] M. García-Hernández,[‡] and J. M. González-Calbet*,[†]

Departamento de Química Inorgánica, Facultad de Químicas, Universidad Complutense, 28040-Madrid, Spain, and Instituto de Ciencia de Materiales, CSIC, Spain

Received January 15, 2009. Revised Manuscript Received March 5, 2009

A tunable hydrothermal synthesis of single-crystalline $BaMnO_3$ nanoparticles is reported. The parameters governing the synthesis pathway are carefully evaluated, assessing their influence on both the morphology and size of the as-prepared products. The reactor filling volume is found to have a main influence on the particle shape (predominance of microrods for a filling volume of 70% and particles for ca 40−50 %), whereas the alkalinity is crucial for the control over the size: higher alkalinities lead to a drastic decrease in both final particle size and aspect ratio. Average minimum particle diameters of ca 20 nm are prepared using a KOH concentration of 20 M, metallic salts concentrations of 50 or 100 mM, and a filling volume of 53%. Finally, the temperature and time exert a minor influence on the final structural properties of the resulting products: 200 °C and lower (even 150°C) and times of 24 hours or less (4 hours) are suitable for nanoparticles formation. The ability to synthesize nanoscale manganites with a narrow particle size distribution has allowed the study of the correlation between the nanoparticle average diameter and magnetic properties. An exchange bias phenomenology is observed in nanosized $BaMnO_3$ as a result of ferromagnetic (FM) correlations in coexistence with a dominant antiferromagnetism. The stronger FM correlations in smaller nanoparticles lead to larger remanence and smaller exchange bias fields.

Introduction

Hydrothermal synthesis is gaining increased interest for the preparation of nanocrystals of binary transition metal oxides given that it offers a wide range of reaction conditions (e.g., temperature, salt and mineralizer concentration, reaction time, etc.) to tailor the composition, shape, and size of the final products. Moreover, the dramatic change in density, ionic product, viscosity, and dielectric constant of water under hydrothermal conditions due to autogenous pressure and high temperature favor the solubility and mobility of species, accessing crystallization reactions that would not occur under conventional conditions.[1] Finally, the one-step and easy handling character of hydrothermal synthesis besides the low temperatures used for reaction makes this procedure a convenient method for the synthesis of not only binary but also multinary metal transition nanooxides.

In spite of its potential, the hydrothermal method has been little employed for the synthesis of nanocrystals of multinary oxides. Although numerous manganese related perovskites or manganites ($A_{1-x}A'_xMn_{1-y}M_yO_{3-\delta}$, AMn_2O_4, $AMn_2O_{5+\delta}$) microcrystals have been synthesized by the hydrothermal method,[2−13] nanomanganites hydrothermally prepared are restricted to $La_{1-x}Ba_xMnO_3$ ($x = 0.3, 0.5, 0.6$) nanocubes[14] and $Ln_{0.5}A_{0.5}MnO_3$ (Ln = La, Pr; A = Ca, Sr, Ba) nanowires.[15−19]

Nanomanganites are a promising system in the field of nanoscience and nanotechnology, as a result of the structural variety and outstanding properties found in their bulk counterparts. The ability of Mn to be stabilized in mixed oxidation states allows many combinations of chemical doping and anion vacancies to be adopted, leading in turn

* Corresponding author. E-mail: jgcalbet@quim.ucm.es. Fax: (34) 91 394 43 52.
[†] Universidad Complutense.
[‡] Instituto de Ciencias de Materiales, CSIC.

(1) Rabenau, A. *Angew. Chem. Int. Ed.* **1985**, *24*, 1026.
(2) Chai, P.; Liu, X.; Wang, Z.; Lu, M.; Cao, X.; Meng, J. *Cryst. Growth Des.* **2007**, *7*, 2568.
(3) Spooren, J.; Rumplecker, A.; Millange, F.; Walton, R. I. *Chem. Mater* **2003**, *15* (7), 1401.
(4) Spooren, J.; Walton, R. I.; Millange, F. *J. Mater. Chem.* **2005**, *15*, 1542.
(5) Liu, J.; Wang, H.; Zhu, M.; Wang, B.; Yan, H. *Mater. Res. Bull* **2003**, *38*, 817–822.
(6) Spooren, J.; Walton, R. I. *J. Solid State Chem.* **2005**, *178*, 1683–1691.
(7) Zhu, J.; Liu, J.; Wang, H.; Zhu, M.; Yan, H. *Cryst. Res. Technol.* **2007**, *42*, 3–241.
(8) Christensen, A. N.; Ollivier, G. *J. Solid State Chem.* **1972**, *4*, 131.
(9) Chen, Y.; Yuan, H.; Li, G.; Tian, G.; Feng, S. *J. Cryst. Growth* **2007**, *305*, 242.
(10) Wang, Y.; Lu, X.; Chen, Y.; Chi, F.; Feng, S.; Liu, X. *J. Solid State Chem.* **2005**, *178*, 1317.
(11) Li, J. Q.; Sun, W. A.; Ao, W. Q.; Tang, J. N. *J. Magn. Magn. Mater.* **2006**, *302*, 463.
(12) Chen, Y.; Yuan, H.; Tian, G.; Zhang, G.; Feng, S. *J. Solid State Chem.,* **2007**, *180*, 167.
(13) Chen, Y.; Yuan, H.; Tian, G.; Zhang, G.; Feng, S. *J Solid State Chem.* **2007**, *180*, 1340.
(14) Urban, J. J.; Ouyang, L.; Jo, M.-H.; Wang, D. S.; Park, H. *Nano Lett.* **2004**, *4* (8), 1547.
(15) Zhu, D.; Zhu, H.; Zhang, Y. *Appl. Phys. Lett.* **2002**, *80*, 1634.
(16) Zhu, D.; Zhu, H.; Zhang, Y. *J. Cryst. Growth* **2003**, *249*, 172.
(17) Zhu, D.; Zhu, H.; Zhang, Y. H. *J. Phys.: Condens. Matter* **2002**, *14*, L519.
(18) Zhang, T.; Jin, C. G.; Qian, T.; Lu, X. L.; Bai, J. M.; Li, X. G. *J. Mater. Chem.* **2004**, *14*, 2787.
(19) Rao, S. S.; Anuradha, K. N.; Sarandi, S.; Bhat, V. *App. Phys. Lett.* **2005**, *87*, 182503.

10.1021/cm9001306 CCC: $40.75
Published on Web 04/06/2009

Table 1. Detailed Reaction Conditions of the Hydrothermal Synthesis of $BaMnO_3$ Nanoparticles and XRD and TEM Results

set	entrant	%autoclav filling	[KOH] (M)[a]	[Ba](mM)[a]	*T* (°C)	time (h)	XRD particle size (101) (nm)	TEM results: morphology and range of particle size[b] (nm)
1	1	**70**	20	100	200	2		nanoparticles; aggregates
	2	**70**	20	100	200	24		nanoparticles/microparticles/ microrods
	3	**70**	2	25	200	24		nanoparticles/microparticles/ microrods/nanoparticles' assemblies in form of microrods
2	4	38	**2**	25	200	24		nanoparticles/microrods 45−750 (ϕ)/150−10000 (L)
	5	38	**2**	50	200	24		nanoparticles/microrods 25−350(ϕ)/ 90−10000 (L)
	6	38	**2**	75	200	24		nanoparticles/microparticles/ microrods
	7	38	**2**	100	200	24		nanoparticles/microparticles/ microrods
3	8	42	8	**50**	200	24		nanoparticles (8−150) nanorods:15−200(ϕ)/80−1000 (L)
	9	48	14	**50**	200	24	30.2	nanoparticles (10−55)
	10	53	20	**50**	200	24	24.9	nanoparticles (8−40)
	11	58	26	**50**	200	24	30.8	nanoparticles (12−139)
4	12	53	**20**	75	200	24	22.2	nanoparticles (11−44)
	13	53	**20**	100	200	24	21.9	nanoparticles (12−41)/microcrystals
5	14	53	20	100	200	**4**	19.9	nanoparticles (6−37)
6	15	53	20	50	**150**	24	20.0	nanoparticles (10−32)/microcrystals

[a] Concentrations listed in the table do not correspond to the final solution because high KOH concentrations provide a significant increase in volume. [b] Size interval containing 90% particles.

to structures with different dimensionality[20] and to interplay among spin, charge, and orbital degrees of freedom.[21−24] Thus, diverse and interesting properties are found in this rich variety of oxides: colossal magnetoresistance in $La_{1-x}A'_xMnO_3$ (A' = alkali earth),[24−28] high permittivity in $BaMn_{0.5}Ti_{0.5}O_3$,[29] multiferroic behaviour and large nonlinear optical response in $BiMnO_3$,[30−33] giant magneto-elastic coupling in multiferroic hexagonal manganites,[34] etc.

We consider that, to date and from a synthetic point of view, neither the variables affecting the shape and size of the products nor their relative relevance have been clearly established in the limited number of works reporting on the hydrothermal synthesis of nanomanganites. Herein, we report a tunable hydrothermal synthesis of single-crystalline nanoparticles of $BaMnO_3$. The optimization of parameters governing this synthesis procedure has allowed to the preparation of monodispersed nanoparticles with minimum sizes in the range of 10−40 nm. The correlation between the nanoparticle average size and magnetic properties is discussed.

Experimental Section

$KMnO_4$ (Aldrich, 99+%), $MnCl_2 \cdot 4H_2O$ (Aldrich, 99.99%), $BaCl_2$ (Aldrich, 99.9 %), and KOH (Merck, pellets, 85 %) were used as-received without further purification. The hydrothermal treatment was performed in a Teflon-lined, aluminium autoclave with a volume of ca. 107 mL. Solutions of each starting material were prepared by dissolving the required amounts of Ba^{2+}, Mn^{2+}, and MnO_4^- salts and KOH (Table 1) in a total volume of 40 mL (sets 2, 3, 4, 5, 6), 50 mL (entrants 1, 2 of set 1) or 66 mL (entrant 3 of set 1) of deionized water. Note that in set #1 a constant filling volume of 70% is achieved for different KOH concentrations by using distinct water amounts. The Ba^{2+}:Mn_{Total} molar ratio was 1:1, according to the nominal composition. The initial mole ratio of the manganese salts was 6 Mn^{2+}:4 MnO_4^- in order to obtain the desired average manganese oxidation state of 4+ in the reaction mixture. The Mn^{2+} and Ba^{2+} solutions were mixed into the Teflon vessel and stirred using a magnetic bar. KOH was added to the resulting homogeneous solution, either as a water solution for samples of low KOH concentration or as pellets for samples of high KOH concentration. Finally, the MnO_4^- solution was added to the solution containing Mn^{2+} and Ba^{2+} salts and KOH. Right after MnO_4^- addition, precipitation of insoluble Mn^{4+}-containing dark-brown oxides can be observed. Because of the appearance of this precipitate, removal of the magnetic bar is recommended before MnO_4^- addition. The Teflon vessel was then placed in a closed autoclave and thermally treated at 200 °C and different reaction times. The detailed reaction conditions and corresponding brief results are summarized in Table 1. After reaction completion, the solution was cooled to room temperature and the resulting green/brown suspensions were centrifugated in order to separate the precipitate from the mother liquid. Excess of alkali impurities were removed by dialysis and the final powder was dried at 50−80 °C overnight.

(20) Mitchell, R. H. *Perovskites Modern and Ancient*; Almaz Press Inc.: Thunder Bay, ON, Canada, 2002.
(21) Millis, A. J. *Nature (London)* **1998**, *392*, 147.
(22) Moreo, A.; Yunoki, S.; Dagotto, E. *Science* **1999**, *283*, 2034.
(23) Tokura, Y.; Nagaosa, N. *Science* **2000**, *288*, 462.
(24) Salamon, M. B.; Jaime, M. *Rev. Mod. Phys.* **2001**, *73*, 583.
(25) Jin, S.; Tiefel, T. H.; McCormack, M.; Fastnacht, R. A.; Ramesh, R.; Chen, L. H. *Science* **1994**, *264*, 413.
(26) Von Helmolt, R.; Wecker, J.; Holzapfel, B.; Schultz, L.; Samwer, K. *Phys. Rev. Lett.* **1993**, *71*, 2331.
(27) Renner, C.; Aeppli, G.; Kim, B.-G.; Soh, Y.-A.; Cheong, S.-W. *Nature (London)* **2002**, *416*, 518.
(28) Loudon, J. C.; Mathur, N. D.; Midgley, P. A. *Nature (London)* **2002**, *420*, 797.
(29) Keith, G. M.; Kirk, C. A.; Sarma, K.; Alford, N. M.; Cussen, E. J.; Rosseinsky, M. J.; Sinclair, D. C. *Chem. Mater.* **2004**, *16*, 2007.
(30) Hill, N. A.; Rabe, K. M. *Phys. Rev. B* **1999**, *59*, 8759.
(31) Moreira dos Santos, A.; Cheetham, A. K.; Atou, T.; Syono, Y.; Yamaguchi, Y.; Ohoyama, K.; Chiba, H.; Rao, C. N. R. *Phys. Rev. B* **2002**, *66*, 064425.
(32) Kimura, T.; Kawamoto, S.; Yamada, I.; Azuma, M.; Takano, M.; Tokura, Y. *Phys. Rev. B* **2003**, *67*, 180401.
(33) Sharan, A.; Lettieri, J.; Jia, Y.; Tian, W.; Pan, X.; Schlom, D. G.; Gopalan, V. *Phys. Rev. B* **2004**, *69*, 214109.
(34) Lee, S.; Pirogov, A.; Kang, M.; Jang, K.-H.; Yonemura, M.; Kamiyama, T.; Cheong, S.-W.; Gozzo, F.; Shin, N.; Kimura, H.; Noda, Y.; Park, J.-G. *Nature (London)* **2008**, *451*, 805.

Powder X-ray diffraction (XRD) patterns were measured using a Siemens D5000 diffractometer with Cu Kα radiation ($\lambda = 1.5418$ Å). Particle size distributions of the powders were measured using dynamic light scattering (DLS) experiments performed using a Malvern instrument, Nano ZS-ZEN3600 fitted with a 630 nm red laser. Samples for DLS measurements were prepared by ultrasonication of the solid (∼0.5 mg) in a 0.1 wt % solution of sodium bis(2-ethylhexyl) sulphosuccinate (AOT) in distilled water (∼5 mL).

Transmission electron microscopy (TEM) was performed on a JEOL JEM-2000 FX electron microscope whereas high-resolution transmission electron microscopy (HRTEM) characterization was carried out using a JEOL300FEG microscope. Chemical composition of the nanocrystals was determined by energy-dispersive X-ray analysis (EDX) in an AN10000 analyzer adapted to both microscopes. Samples for TEM and HRTEM were prepared by adding 1−2 drops of an *n*-butanol suspension onto a copper grid covered by an amorphous carbon film.

Magnetization measurements on fresh samples were obtained by SQUID magnetometry using a Quantum Design magnetometer equipped with a 5 Tesla superconducting coil. The temperature range explored is (2−400 K).

Results and Discussion

As previously mentioned, the aim of this work is to optimize the parameters determining the achievement of nanomanagnites under hydrothermal conditions. Since the seminal work published in 1972 by Christensen and co-workers,[8] there has been a single paper reporting on the hydrothermal synthesis of tablet-shaped $BaMnO_3$ crystallites with lengths ranging from ∼0.5 to 2 μm.[6] The experimental conditions used in this case (i.e., a combination of both high KOH and metallic salts concentrations with barium and manganese concentrations of ∼222 mM and KOH concentration of ∼40 M) failed in the achievement of nanometer-sized particles, most likely because (i) reactants were not soluble enough for creating a homogeneous medium at supersaturation and/or (ii) first nuclei tend to aggregate and sinter.

The experimental conditions for the synthesis of $La_{1-x}Ba_xMnO_3$ nanoparticles with different doping levels have been the most widely explored. A close inspection of these works allows two synthetic conditions to be distinguished for the achievement of (i) nanowires of 30−150 nm diameter and tens of micrometers length for [KOH] = 10 M and [metallic salts concentrations] = 284 mM,[15] and (ii) nanometer-sized cubes of 50−100 nm diameter for [KOH] = 12 M and [metallic salts concentrations] = 100 mM.[14] These close reaction conditions make it quite difficult to establish any correspondence between morphology and concentrations. Actually, both concentrations were also slightly lower than those described above for the synthesis of $BaMnO_3$, where microparticles (rather than nanoparticles or nanowires were obtained). More recently, Chai et al[2] have observed that the increase on the KOH concentration from 6 up to 14 M leads to a drastic decrease of the final particle size of $La_{0.5}Ba_{0.5}MnO_3$; e.g., for KOH 14 M, microcubes of 100−450 nm are obtained, whereas for 10 M, the particle size increases up to 0.5−2 μm; finally, for [KOH] = 6 M, flowerlike particles of 5−15 μm diameter are obtained.

On the basis of the above mentioned results, we consider it highly desirable to study the influence of the experimental conditions used to carry out the hydrothermal synthesis on the morphology (e.g. micro/nanoparticles or nanowires) of the resulting manganites. A careful inspection to those works reporting on nanoparticles and nanowires revealed that the most significant difference among them was the reactor filling volume (e.g., ∼70 % for $La_{0.5}Ba_{0.5}MnO_3$ nanowires[12] and ∼33 % for nanocubes[14]). Thus, we first aimed to reproduce the synthetic conditions described by Zhu and co-workers (in terms of reactor filling volume) for preparation of $BaMnO_3$ nanowires within a certain range of KOH and metal salts concentrations (see Table 1, set 1). The temperature of the reactions was fixed at 200 °C (autoclave filling around 70%), whereas the influence of the reaction time in the final products was also evaluated. All the obtained samples exhibit the XRD patterns corresponding to the 2H-structure of $BaMnO_3$, as shown in Figure 1. The symmetry and calculated lattice parameters are consistent with the bulk values (a = 5.6990 Å, c = 4.8170 Å, $P6_3/mmc$).[35]

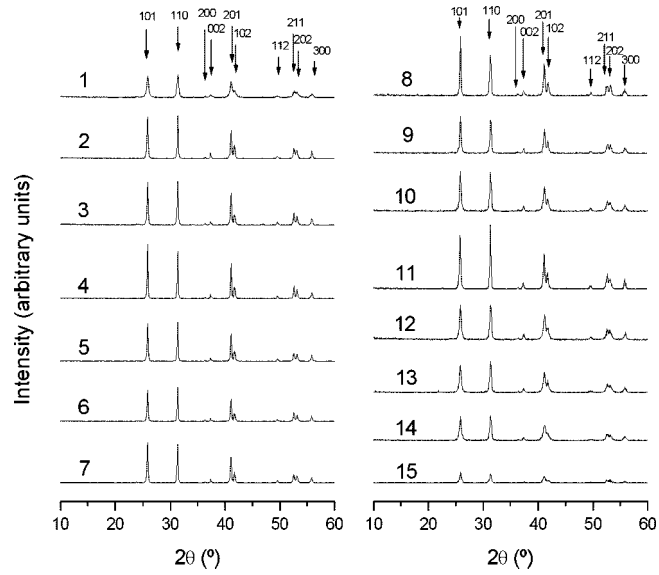

Figure 1. XRD patterns corresponding to all samples depicted in Table 1. All of them are monophasic and can be assigned to the $BaMnO_3$ unit cell.

The cationic composition, determined at the nanoscale level by EDX after analyzing around 30−40 crystallites, reveals a stoichiometric 1.0:1.0 ratio for Ba:Mn within experimental errors, in good agreement with the nominal composition.

TEM micrographs (Figure 2) show that in all cases, the morphology of the resulting $BaMnO_3$ is somewhat heterogeneous, ranging from microparticles to microrods, no matter the reaction time or KOH metal salt concentrations. Regardless of the unsuccessful achievement either of $BaMnO_3$ nanoparticles or nanorods in any of these samples, the $BaMnO_3$ synthesized using the lowest KOH and metallic salts concentrations provide quite interesting information with regards to the formation mechanism of microrods: self-assembly of acicular $BaMnO_3$ nanoparticles. Such assembly is shown in the TEM image of the sample 4 (Figure 3a). The corresponding electron diffraction pattern (Fig. 3b) reveals the monocrystalline character of this assembly.

(35) Chamberland, B. L.; Sleight, A. W.; Weiher, J. F. *J. Solid State Chem.* **1970**, *1*, 506.

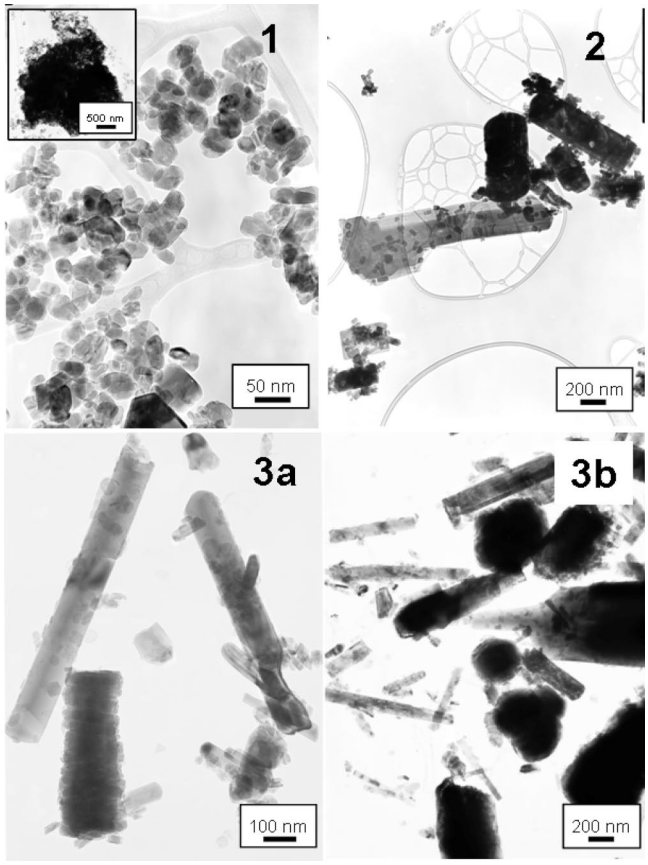

Figure 2. TEM micrographs of $BaMnO_3$ samples 1, 2 and 3. These samples correspond to a constant autoclave filling of 70%. The formation of nano/microrods by self-assembly of nanoparticles seems to be favored under this condition.

Actually, all the observed maxima can be indexed on the basis of the hexagonal unit cell of the 2H-$BaMnO_3$ along the [100] zone axis. This result indicates that all the nanoparticles are oriented along the same direction, corroborating that the observed assembly is an intermediate in the microrod formation.

The presence of small nanoparticles as intermediates of the large microrods is also encouraging for the achievement of isolated nanoparticles; one should just determine the synthethic conditions to avoid aggregation. As mentioned above, the particle shape seems to be mostly related to the reactor filling volume. So to determine the influence of this variable, our next sets of samples were prepared from solutions filling ca. 40% of reactor volume. In the first set of samples (set #2), KOH concentration was fixed at 2 M, and metallic salts concentration ranged from 25 to 100 mM. For concentrations of 25 and 50 mM, mixed microrods and nanoparticles with broad particle size distributions were obtained. In both cases, the nanoparticles size ranged from 25 to above 100 nm, whereas rods were slightly smaller for a metallic salt concentration of 50 mM (25−350 nm diameter and 90−1000 nm length) than for that of 25 mM (45−750 nm diameter and 150−1000 nm length). Besides, it is worth noting that further aggregation tendency is observed for the 50 mM sample. Further increase in concentration (e.g., 75 and 100 mM) leads to very inhomogeneous samples with predominance of aggregated particles (of undefined shape)

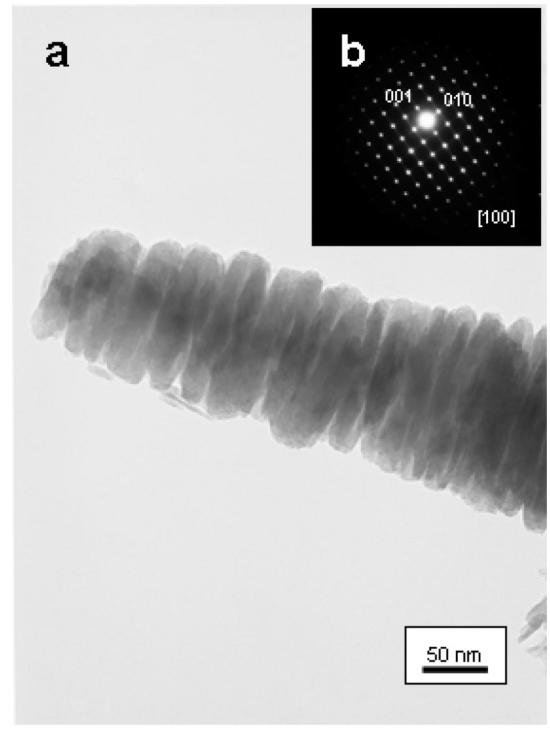

Figure 3. (a) TEM micrograph of self-assembled acicular $BaMnO_3$ nanoparticles into a microrod. (b) Corresponding SAED pattern, showing the monocrystalline character of the assembly. Such formations are characteristic of sample 3 (Table 1).

at the micrometer scale and some wide rods (200 nm diameter). Representative TEM images are shown in Figure 4.

The above results seem to indicate that aggregation of primary particles tends to be favored in a solution rich in metallic salts and low ionic strength. Because a KOH concentration of 2 M failed in avoiding aggregation (in form of both large particles and microwires) and hence to obtain uniform nanoparticles, in our next set of samples (set #3), the metallic salts concentration was fixed at 50 mM and the filling volume was kept close to 50%, whereas the KOH concentration varies from 2 to 26 M. First, the increase in the KOH concentration from 2 M (sample 5) to 8 M (sample 8) results in partial disappearance of aggregates and in a decreasing of the particle size, though rods and particles remain in coexistence (Figure 5, sample 8). Further KOH increase (14 and 20 M) gives rise to isolated nanoparticles (Figure 5, samples 9, 10). The high-resolution TEM image (Figure 6a) and the Fourier Transformation pattern (Figure 6b) of the resulting $BaMnO_3$ nanoparticles show a single crystalline nature, corresponding to the 2H structural type. The micrograph was taken along the 010 zone axis; in this zone, the structure is viewed parallel to the columns of Ba−O close-packed rows and the stacking sequence of the layers is revealed directly. By considering that Ba atoms are projected as brighter dots, the experimental contrast is associated with a (hh) layered sequence. A calculated image with the ideal atomic positions corresponding to a 2H polytype (see inset in Figure 6a) fits well with the experimental image for $\Delta t = 5$ nm, $\Delta f = -500$ nm.

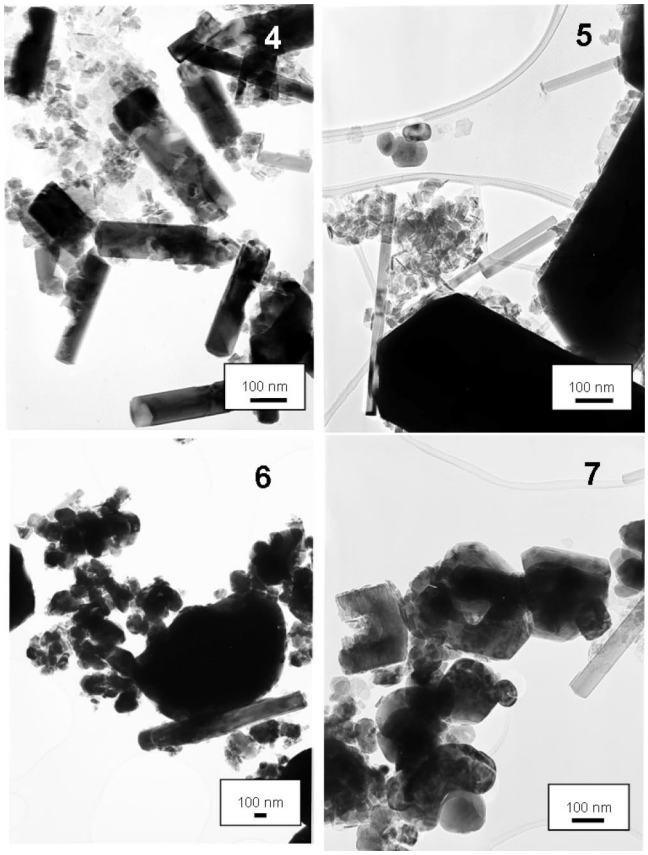

Figure 4. TEM micrographs of $BaMnO_3$ samples 4, 5, 6, and 7 of Table 1, corresponding to a fixed KOH concentration of 2 M, fixed autoclave filling ca. 40%, and metallic salts concentration of 25 (4), 50 (5), 75 (6), and 100 mM (7).

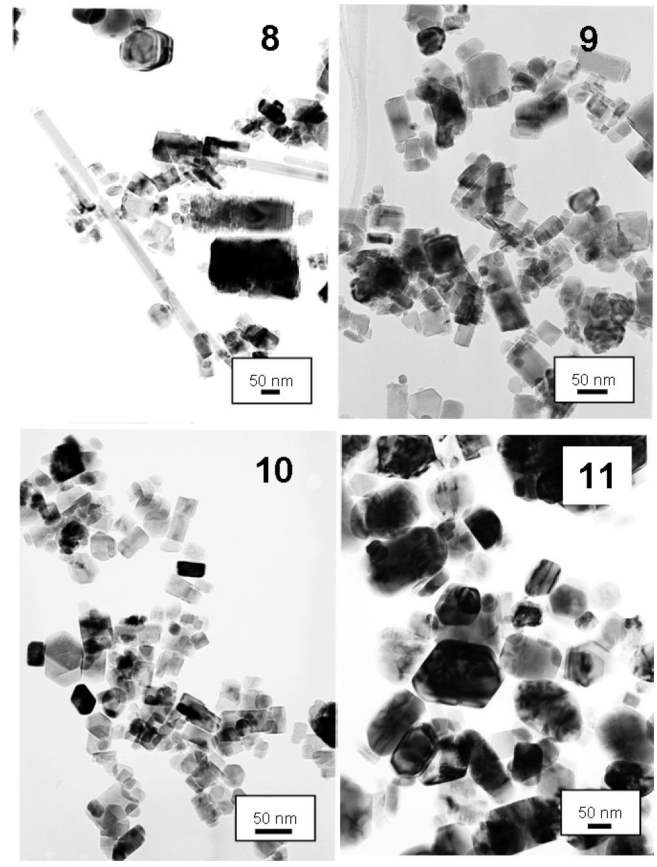

Figure 5. TEM micrographs of $BaMnO_3$ samples 8, 9, 10, and 11 (see Table 1), corresponding to a fixed metallic salts concentration of 50 mM, filling volume of ca. 50 %, and KOH concentrations of 8 (8), 14 (9), 20 (10), and 26 M (11). Note that the increase in KOH concentration from 8 to 20 M leads to a decrease in both particle size and aspect ratio of the resulting nanoparticles.

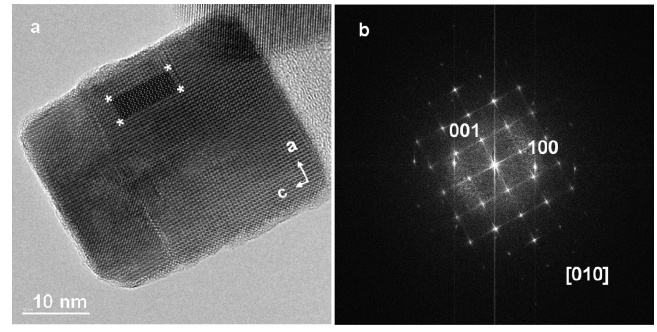

Figure 6. (a) HRTEM image of a ca. 30 nm × 37 nm $BaMnO_3$ nanoparticle along the 010 zone axis corresponding to sample 10 of Table 1. Simulated image is shown in the inset. (b) Corresponding Fourier transformation pattern.

Further insights about synthesized $BaMnO_3$ nanoparticles (e.g., mean particle size, particle size distribution) were provided by dynamic light scattering measurements (DLS). Figure 7 depicts a narrow particle size distribution with mean particle size centred at 37 nm for sample 13, a value slightly larger than that average value estimated by TEM (e.g., ∼26 nm). Such discrepancy can be ascribed to the eventually larger hydrodynamic volume of AOT coated nanoparticles (remind AOT was used for nanoparticle resuspension, see experimental). Besides, sizes determined by TEM images were based on the minimal dimension of the nanoparticles, while the size detected by dynamic light scattering measurements is related with the diameter of the corresponding hydrodynamic sphere. Note that $BaMnO_3$ nanoparticles exhibit certain acicular form in each of the synthesized samples. Interestingly, DLS measurements allowed discarding the presence of large aggregates and microcrystals in each of the selected samples, in good concordance with TEM micrographs.

An overall analysis of the above results reveals the different relevance of studied parameters on the final $BaMnO_3$ particle size. From these, the KOH concentration appears as the most significant one in the achievement of isolated nanoparticles of $BaMnO_3$. On one hand, KOH favors the homogenous dissolution of metallic salts thanks to the high ionic strength of the solution, whereas on the other, it helps for inhibition of uncontrolled growth of first nucleus by aggregation processes. Note that two typical growth mechanisms, ion-to-ion attachment[36,37] and self-assembly of nanocrystals,[38] are both hampered; the former because of the lack of remaining Ba^{2+} and Mn^{4+} cations in solution and the latter because of electrostatic repulsion of nanoparticles (OH^--surface-charged at high pH levels). The third most typical growth mechanism (e.g., Ostwald-like ripening pro-

(36) Cushing, B. L.; Kolesnichenko, V. L.; O'Connor, J. *Chem. Rev.* **2004**, *104*, 3893–3946.
(37) Park, J.; Joo, J.; Kwon, S. G.; Jang, Y.; Hyeon, T. *Angew. Chem., Int. Ed.* **2007**, *46*, 4630–4660.
(38) Niederberger, M.; Cölfen, H. *Phys. Chem. Chem. Phys.* **2006**, *8*, 3271–3287.

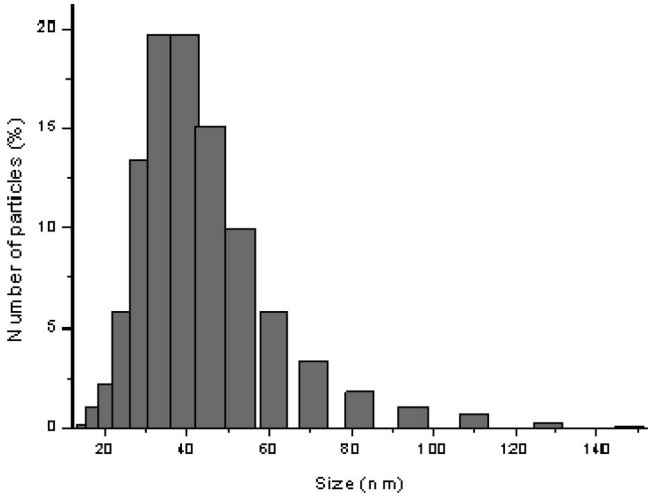

Figure 7. Particle size distribution of sample 13 measured by dynamic light scattering (DLS). The size distribution is centred at 37 nm.

cess[39]) also seems to be disfavored, most likely because of the poor solubility of smallest crystallites in such an alkaline solution. Actually, the use of 14−20 M KOH concentrations allowed for the achievement of $BaMnO_3$ nanoparticles even for metallic salts concentrations of 75−100 mM (Figure 8, samples 12, 13), opposite the large aggregates found for KOH 2 M (Figure 4, samples 6, 7). Nonetheless, metallic salt concentrations ranging from 75 to 100 mM (set 4 in Table 1; Figure 8, samples 12, 13) kept exhibiting a strong tendency to aggregate even for KOH 20 M, so that the achievement of single nanoparticles required of shorter reaction times (4 h; set 5 in Table 1; Figure 8, sample 14). It should also be noted that decreasing particle size was accompanied by decreasing aspect ratio of the final particles (compare samples 8 and 10, Figure 5). This tendency has also been reported for hydrothermally synthesized $La(OH)_3$ nanorods.[40] Finally, at KOH concentrations of 26 M (sample 11), the above-mentioned trend changes and microparticles of average size of 59 nm are obtained. It is worth stressing that KOH may also play an additional role in the synthesis of $BaMnO_3$ because of the formation of an intermediate, a birnessite-type phase $K_{0.5}MnO_2 \cdot nH_2O$ having the desired Mn oxidation state in between the $[MnO_4]^{4-}$ and Mn^{2+} precursors, by coproportionation reaction between $[MnO_4]^{4-}$ and Mn^{2+}.[4]

The achievement of $BaMnO_3$ nanoparticles of ca. 26−37 nm by hydrothermal synthesis is remarkable. Not only because $BaMnO_3$ nanoparticles have not been reported up to now but, even more, because the smallest nanomanganites reported to date (also by hydrothermal synthesis)[14]in other manganese-related systems, e.g., $La_{0.5}Ba_{0.5}MnO_3$, were larger (ca. 50−100 nm) and the particle size distribution broader. Furthermore, Urban et al[14] used a higher temperature than we did (300 versus 200 °C), but it is worth noting that increased temperatures might be required given the different composition of the nanomanganites ($La_{0.5}Ba_{0.5}MnO_3$ and $BaMnO_3$). Nonetheless, the use of lower temperatures is of tremendous interest for practical applications, making the synthesis more affordable in terms of energy and equipment (note that temperatures below 240 °C allow for the use of reactors having Teflon inner containers). Given the relevance of this issue, we further explored the suitability of hydrothermal synthesis at even lower temperatures (e.g., 150 °C, set #6, and sample 15 in Figure 8). TEM micrographs and XRD revealed that this low temperature was high enough for the preparation of single $BaMnO_3$ nanoparticles of ca. 20 nm.

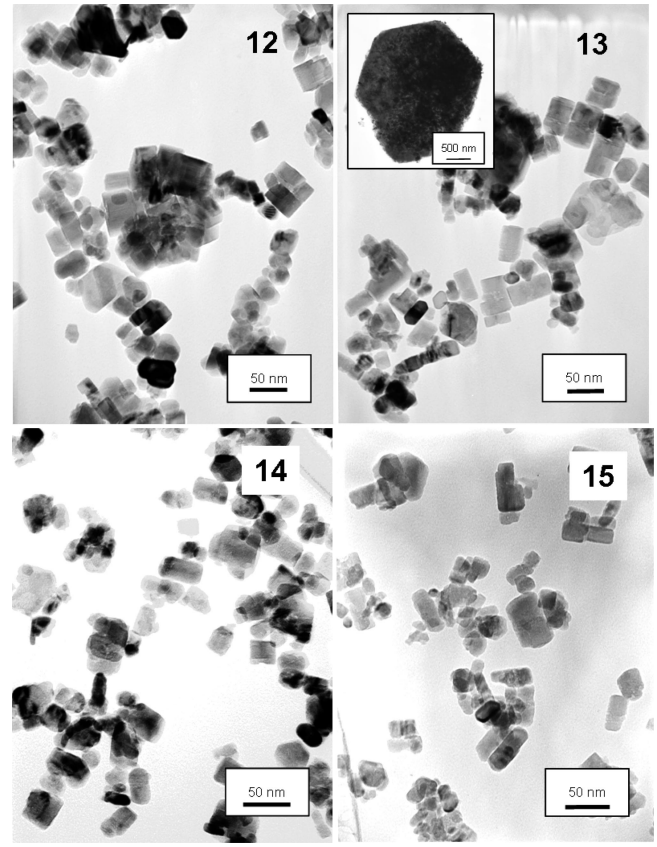

Figure 8. TEM micrographs of $BaMnO_3$ samples 12, 13, 14 and 15 of Table 1, corresponding to a fixed KOH concentration of 20 M. Comparison of images 12 and 13 show the small influence of metallic salts concentration. Aggregation and microcrystals favored at those metallic salts concentrations can be avoided by using shorter reaction times: (12), 24 h. and (14), 4 h. Temperatures as low as 150 °C are suitable for the synthesis of $BaMnO_3$ nanocrystals (sample 15).

To study the influence of the particle size in the magnetic properties, we performed a full characterization of 2H-$BaMnO_3$ using squid-magnetometer techniques. We recorded zero-field-cooled and field-cooled (ZFC-FC) scans, as well as 5 K isotherms under several conditions, in searching for an exchange bias phenomenology so specific of antiferromagnetic materials in intimate contact with ferromagnetic layers/patches.[41] This is to be expected if surface magnetism plays an important role, as is the case in nanoparticles composed by a core magnetically different from the outer layers or, alternatively, if there exists a number of uncompensated spins on a *n*-sublattice model in which the reduced coordination of surface spins leads to fundamental changes in the magnetic order throughout the particle.[42]

(39) Boistelle, R.; Astier, J. P. *J, Cryst. Growth* **1988**, *90*, 14–30.
(40) Wang, X.; Li, Y. *Angew. Chem., Int. Ed.* **2002**, *41* (24), 4790–4793.
(41) Nogués, J.; Sort, J.; Langlais, V.; Skumryev, V.; Suriñach, S.; Muñoz, J. S.; Baró, M. D. *Phys. Rep.* **2005**, *422*, 65–117.

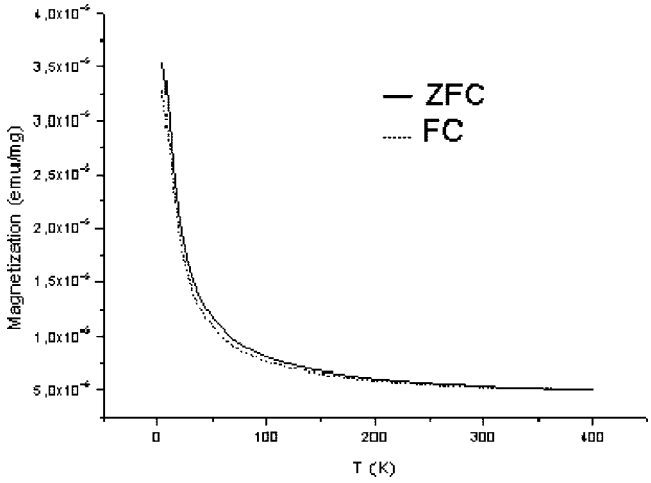

Figure 9. Representative plot (sample 10) of a ZFC-FC run of the magnetization versus temperature, as measured under 1000 Oe cooling and measuring field.

From magnetometry and neutron diffractions data, it has been reported that the bulk behaviour of 2H-$BaMnO_3$ exhibits the basic characteristics of an antiferromagnet, although no obvious antiferromagnetic peak is spotted in the temperature dependence of the magnetization.[8]

Figure 9 shows a representative (sample 10) plot of a ZFC-FC run of the magnetization versus temperature, as measured under 1000 Oe cooling and measuring field. The absence of singularities as well as a modest irreversibility is the most remarkable feature. As already mentioned, the ocurrence of an antiferromagnetic transition has been reported for bulk $BaMnO_3$. However, the nature of the AF ordering has been strongly debated. Although Christensen and Ollivier[8] proposed a collinear AFM model to fit their neutron diffraction (ND) data, Cussen and Battle,[43] from higher-resolution ND patterns, demonstrate the existence of canting. This canting in the *xy* plane would be a consequence of the triangular lattice formed by the Mn cations. Also, there is no consensus about the Néel temperature of the transition. Christensen and Ollivier locate the transition bellow 2.4 K, whereas the Cussen and Battle measurements render $T_N = 59$ K. The latter authors take the high T_N as a strong point against the 1D character of the AF of 2H-oxides bellow room temperature, suggesting that the intrachain magnetic interactions cannot be considered negligible as compared to the intrachain interactions. However, the proposed 3D ordering below 59 K does not translate into a maximum in the *M* vs. *T* data, contrary to what it is expected for a long-ranged three-dimensional AF ordering. Christensen and Ollivier put forward the existence of a partial AFM order below 150 K and conjecture that a 1D AFM could be at the origin of their observations. Discrepancies between both groups could possibly be ascribed to the very different systhesis methods followed.[8,43] Our data in Figure 9 are more in accordance with those reported by Christensen and Ollivier because no hint of an AFM transition can be seen in the *M* vs. *T* plot, down to the lowest temperature explored (2 K).

From our data, the existence of some kind of ferromagnetic correlations is established in Figure 10, where representative hysteresis cycles measured at $T = 2$ K recorded after a 1000 Oe cooling and after a 20 kOe are depicted.

Two distinct characteristics are already apparent: although saturation is not reached, the cycle opens up rendering non-zero remanence and coercive field. Also a clear exchange bias (displacement of the center (0,0) of the hysteresis cicle when cooling the system under an applied external field), pointing out that the Néel transition has already taken place at this temperature. Both facts points toward the coexistence of FM correlations in addition to the dominant antiferromagnetism. From considerations about the role of uncompensated spins in the nanoparticle surface, it is plausible to think that our observations are a direct consequence of the downsizing of particles[44] and that our synthesis pathway has rendered an assembly of particles with dominant AFM correlations and some kind of FM interactions. Whether the FM fraction is located at the surface or it does exist throughout the nanoparticle is unknown but the interaction between the AFM and FM fractions is clearly assessed by the observed exchange bias effects.

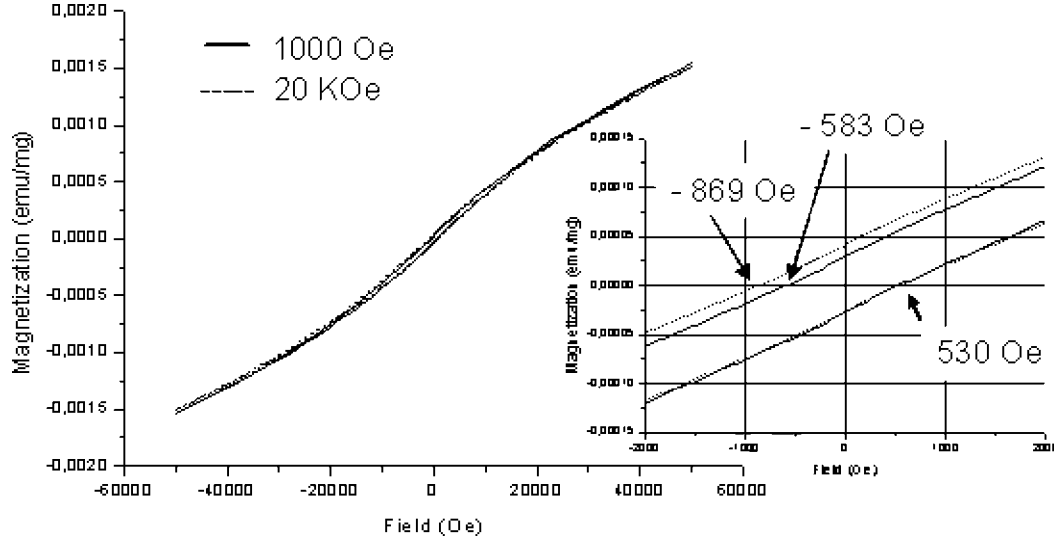

Figure 10. Representative hysteresis cycles (sample 14) measured at $T = 2$ K, recorded after a 1000 Oe and after a 20 kOe field cooling protocol. Inset: close up of the central region.

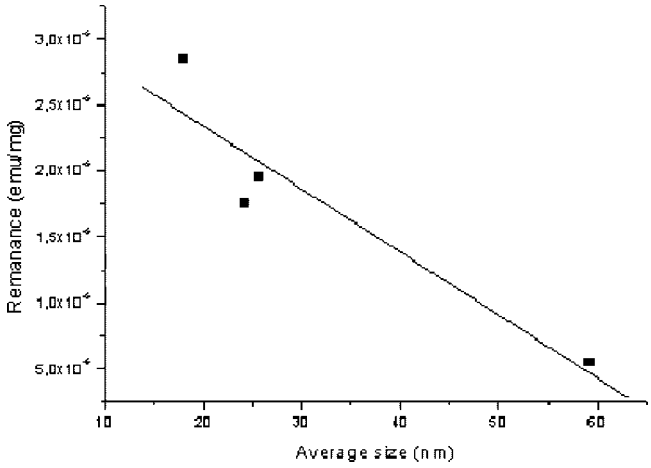

Figure 11. Remanence (emu/mg) vs average diameter (nm). The straight line should be interpreted only as a guide for the eye.

Although the distribution of particle size is not monodisperse in our samples, it is possible to extract some information on the average diameter dependence of the remanence, as it is shown in Figure 11. As the particle size decreases the remanence increases, pointing out that a stronger and larger ferromagnetic fraction develops. This is consistent with the fact that the smallest nanoparticle shows larger surface/volume ratios: smaller particles must contain a larger number of uncompensated spins in one of the sublattices of the antiferromagnet, enabling stronger FM correlations. The same behavior is observed from the measured magnetization at the highest measured field (50 KOe) (not shown).

An inverse trend is observed in the variation of the exchange bias field, H_{eb}, with the average size of the particles, as measured at 2 K after a 2 T field cooling. Small particles exhibit smaller H_{eb} than the large particles (160 Oe and 363 Oe for 18-sample 14-and 59 nm-sample 11-average diameters, respectively). This is consistent with a weakening of the AFM interactions and enhancement of the FM interactions when the particle size decreases. As the diameter is reduced, AFM interactions become less efficient to induce exchange bias effects at a given temperature, as a result of a lower blocking temperature or a lower anysotropy.

Conclusions

In this work, we have performed a careful study of the features governing 2H $BaMnO_3$ nanocrystals synthesis and stabilization under hydrothermal conditions. Thus, high KOH concentration has been found to be crucial for the synthesis of nanoparticles by both promoting fast precipitation of first nuclei and charging their surface (OH^- anions attachment) that ultimately impedes nanoparticles aggregation. Meanwhile, metallic salt concentrations have a minor influence on final particle size and their increase (within the studied range) exhibited a certain tendency to favor aggregation and sintering effects. In any case, such a tendency can be hampered by using shorter reaction times. In regards to the reaction temperature, the study has demonstrated that temperatures of 200 °C and below (even 150 °C) are enough for nanoparticle formation, with minor differences on final particle size distribution. In particular, nanoparticle diameters have been finely tuned within the range ~18−59 nm depending on the reaction parameters, while preserving narrow size distributions in every case. The good control on the particle size distribution within the nanometer scale has also allowed for the achievement of preliminary investigations of the size-dependent evolution of the magnetic phenomena in this family of compounds.

We consider that the decrease in the synthesis temperature to 150 °C, besides the good particle size control even for high precursor concentrations, opens the path for the consolidation of hydrothermal synthesis as a suitable route to prepare not-agglomerated, surface-free 2H $BaMnO_3$ nanocrystals and, eventually, of other types of mixed manganese oxide nanocrystals (e.g., $La_xBa_{1-x}MnO_3$).

Acknowledgment. Financial support through research Projects MAT2007-61954 (Ministerio de Ciencia e Innovación (MCINN), Spain) and PR34/07-15855 (Santander-Universidad Complutense, Spain) are acknowledged. A.Q. thanks the MCINN for financial support through a postgraduate grant.

CM9001306

(42) Kodama, R. H.; Berkowitz, A. E. *Phys. Rev. Lett.* **1999**, *59*, 6321.
(43) Cussen, E. J.; Battle, P. D. *Chem. Mater.* **2000**, *12*, 831.
(44) Néel, L. In *Low Temperature Physics*; De witt, C., Dreyfus, B., De Gennes, P. D., Eds.; Gordon and Beach: New York, 1962; p 213.